Physics in Medicine & Biology

PAPER • OPEN ACCESS

Real-time dose reconstruction in proton therapy from in-beam PET measurements

To cite this article: V V Onecha *et al* 2025 *Phys. Med. Biol.* **70** 075008

IOP Publishing Phys. Med. Biol. 70 (2025) 075008 https://doi.org/10.1088/1361-6560/adbfd9

Physics in Medicine & Biology

IPEM Institute of Physics and Engineering in Medicine

PAPER

Real-time dose reconstruction in proton therapy from in-beam PET measurements

V V Onecha[1,2,4], A Espinosa-Rodriguez[1,2,*], C Soneira-Landín[1,2], F Arias-Valcayo[1,2], S Gaitán-Dominguez[1,2], V Martinez-Nouvilas[1,2], M García-Díez[1,2], P Ibáñez[1,2], S España[1,2,5], D Sanchez-Parcerisa[1,2], F Cerrón-Campoo[3], J A Vera-Sánchez[3], A Mazal[3], J M Udias[1,2] and L M Fraile[1,2]

[1] Grupo de Física Nuclear, EMFTEL & IPARCOS, Universidad Complutense de Madrid, Madrid, Spain
[2] Instituto de Investigación del Hospital Clínico San Carlos (IdISSC), Ciudad Universitaria, Madrid, Spain
[3] Centro de Protonterapia Quirónsalud, Madrid, Spain
[4] Present address: Massachusetts General Hospital & Harvard Medical School, Boston, United States of America
[5] Present address: Instituto de Tecnologías Físicas y de la Información 'Leonardo Torres Quevedo' (ITEFI), Consejo Superior de Investigaciones Científicas (CSIC), Madrid, Spain
[*] Author to whom any correspondence should be addressed.

E-mail: anespi04@ucm.es

Keywords: proton therapy, online dose reconstruction, online range verification, proton dose reconstruction, online activity reconstruction, IDE-PET

Supplementary material for this article is available online

OPEN ACCESS

RECEIVED
24 December 2024

REVISED
3 March 2025

ACCEPTED FOR PUBLICATION
12 March 2025

PUBLISHED
21 March 2025

Abstract

Objective. Clinical implementation of in-beam positron emission tomography (PET) monitoring in proton therapy (PT) requires the integration of an online fast and reliable dose calculation engine. This manuscript reports on the achievement of real-time reconstruction of 3D dose and activity maps with proton range verification from experimental in-beam PET measurements. *Approach*. Several cylindrical homogeneous PMMA phantoms were irradiated with a monoenergetic 70 MeV proton beam in a clinical facility. Additionally, PMMA range-shifting foils of varying thicknesses were placed at the proximal surface of the phantom to investigate range shift prediction capabilities. PET activity was measured using a state-of-the-art in-house developed six-module PET scanner equipped with online PET reconstruction capabilities. For real-time dose estimation, we integrated this system with an in-beam dose estimation algorithm, which combines a graphical processing unit-based 3D reconstruction algorithm with a dictionary-based software, capable of estimating deposited doses from the 3D PET activity images. The range shift prediction performance has been quantitatively studied in terms of the minimum dose to be delivered and the maximum acquisition time. *Main results*. With this framework, 3D dose maps were accurately reconstructed and displayed with a delay as short as one second. For a dose fraction of 8.4 Gy at the Bragg peak maximum, range shifts as small as 1 mm could be detected. The quantitative analysis shows that accumulating 20 s of statistics from the start of the irradiation, doses down to 1 Gy could be estimated online with total uncertainties smaller than 2 mm. *Significance*. The hardware and software combination employed in this work can deliver dose maps and accurately predict range shifts after short acquisition times and small doses, suggesting that real-time monitoring and dose reconstruction during PT are within reach. Future work will focus on testing the methodology in more complex clinical scenarios and on upgrading the PET prototype for increased sensitivity.

1. Introduction

Proton therapy (PT) has seen exponential growth over the last decades due to its dosimetric advantages. Protons deposit most of their dose at the end of their range in the so-called Bragg peak, precisely targeting the tumor while sparing healthy tissues. However, this feature also makes treatments more sensitive to

uncertainties, underscoring the importance of an accurate ion-range verification protocol to ensure a correct dose delivery and reduce safety margins (Paganetti 2012).

Positron emission tomography (PET) has been extensively proposed for *in vivo* PT range verification. It is based on the detection of β^+ isotopes generated by protons through nuclear reactions in the irradiated regions (Parodi *et al* 2007). Activation maps obtained with a PET system can then be correlated to maps of the deposited dose in the patient. In clinical practice, PET imaging can be implemented following three different strategies: (i) offline PET, where the patient is scanned outside the treatment room shortly after irradiation, (ii) in-room PET, where the patient is scanned immediately after treatment but still inside the room, and (iii) in-beam PET, where the scanner is fully integrated in the treatment delivery system allowing data acquisition to take place during irradiation. In-beam PET is naturally more attractive as it provides immediate feedback, allows for the detection of intra-fractional errors and thanks to the minimal elapsed time between the β^+ isotope formation and its detection, reduces the impact of biological washout (Shakirin *et al* 2011), which becomes relevant after 2–5 min post-irradiation (Toramatsu *et al* 2018, 2022). Some examples of clinical in-beam PET systems proposed to date include the trailblazing double-head PET camera installed at GSI (Darmstadt, Germany) (Enghardt *et al* 2004a), the Beam ON-LINE PET system (BOLPs-RGp) at the National Cancer Center, (Kashiwa, Japan) (Nishio *et al* 2010), the dual-head INSIDE PET system at the National Center of Oncological Hadrontherapy (CNAO) (Bisogni *et al* 2017), the full-ring detector OpenPET (Tashima *et al* 2020), or the ibPET (Kong *et al* 2024). Other in-beam PET systems are currently under development at several clinical centers, such as the Linkou Chang Gung Memorial Hospital (Taoyuan, Taiwan) (Gao *et al* 2020), the University of Texas Southwestern Medical Center (Dallas, TX, USA) (Yang *et al* 2021) the Lausanne University Hospital (Lausanne, Switzerland) (Makkar *et al* 2022), and the MD Anderson Cancer Center (Houston, TX, USA) (Abouzahr *et al* 2023).

For a successful application in the clinics, these detection systems must meet several requirements (Parodi *et al* 2023). First, in-beam PET systems are challenged by significant background radiation, characteristic of the beam-on period. Therefore, dedicated readout electronics must be developed, in combination with state-of-the-art detectors, to build systems with high count-rate capabilities and digital signal processing performance, to perform high-resolution real-time measurements of position, time, and energy without loss of data. Additionally, the system readout bandwidth and data storage capacity should be sufficiently large to avoid event losses during data transmission (Yan *et al* 2023). Real-time signal processing implementation for in-beam PET has been widely explored in several works (Ke *et al* 2021, Yang *et al* 2021, 2024, Yan *et al* 2023).

Second, the beam delivery system and the position of the patient couch and other medical devices in the treatment room set stringent boundary conditions on the geometry of the in-beam PET scanner (Crespo *et al* 2006, Sanaat *et al* 2024). This yields atypical scanner configurations, including cylindrical, dual-head (Enghardt *et al* 2004a, Nishio *et al* 2010, Camarlinghi *et al* 2014, Bisogni *et al* 2017, Kong *et al* 2024) or a combination of both (Brzezinski *et al* 2023, Yang *et al* 2024). Open-type geometries, such as slant-ellipsoid, axial-shift single-full-ring (Tashima *et al* 2016), dual-full-ring (Yamaya *et al* 2008), or half-rings (Montarou *et al* 2017), face restricted angular coverage, often leading to significant image noise and artifacts in reconstructed images. To mitigate such effects, specialized reconstruction algorithms are essential (Sanaat *et al* 2024), for instance taking into account the spatially varying and asymmetrical nature of the actual point spread function (Arias-Valcayo *et al* 2023). Ideally, the image reconstruction algorithm should be integrated in real-time and be fast enough to provide prompt feedback of the PET activity in the patient. This can be achieved using graphical processing units (GPUs). Pioneering work in this area has been done with the INSIDE (Innovative Solution for Dosimetry in Hadrontherapy) system (Ferrero *et al* 2018), where an on-the-fly reconstruction algorithm has been implemented, offering a time resolution of about 10 s, with an average delay of 6 s between the delivery and the availability of the reconstructed image.

It should be underlined that, when PET methods are used for range verification in PT, the activity and the dose distributions are non-linearly correlated, since they arise from different physical processes. This makes deriving dose maps from measured activity maps a challenging task. Consequently, this remains an open issue, and current approaches rely on empirical methods that derive the particle range inside the patient solely from the PET distribution (Kraan *et al* 2022, Moglioni *et al* 2022, Brzeziński *et al* 2023).

However, real-time dose monitoring has the potential to decrease range uncertainty, thereby allowing for a reduction of the safety margins around the tumor and enabling online plan modifications in case of target over or underdosing. Several attempts have been made to translate measured activities into deposited doses (Parodi *et al* 2006, Fourkal *et al* 2009, Remmele *et al* 2011, Liu *et al* 2019), with only one of the systems implemented clinically (Parodi *et al* 2007). Most of the algorithms in use have limited accuracy and lack a 3D dose calculation algorithm. Other limitations in previous PET systems arise from the incompatibility of the software architecture, which allowed dose reconstructions only after a considerable time span, as opposed to real-time implementations.

In a previous work (Onecha *et al* 2022), we proposed a method for fast 3D dose reconstruction from in-beam PET data, which relied on a realistic pre-calculated dose-activity dictionary (DAD) obtained via Monte Carlo simulations, combined with a GPU implementation of the maximum likelihood expectation-maximization (MLEM) and simulated annealing (MSA) algorithm. Hence, the resulting dose distribution was noiseless and could be obtained in a near-instantaneous fashion. This in-silico investigation (Onecha *et al* 2022) supported the feasibility of estimating the proton range with submillimeter accuracy with clinical doses down to 1 Gy.

In the present paper, we demonstrate for the first time the feasibility of real-time dose reconstruction from in-beam PET data obtained from clinical proton beams. To this end, we propose a new In-beam Dose Estimation tool from PET (IDE-PET), which combines a fast GPU-MLEM activity reconstructor with the DAD-MSA algorithm. Experiments performed using an in-house developed six-module PET scanner by irradiation of PMMA phantoms at the Quirónsalud PT Center (Madrid, Spain) provide reliable 3D dose maps in approximately 2 s.

2. Materials and methods

2.1. MiniPET scanner

A benchtop in-beam PET scanner, coined MiniPET, has been developed in-house in collaboration with SEDECAL (Sociedad Española de Electromedicina y Calidad, S.A) (Espinosa-Rodriguez *et al* 2024). Its configuration is based on the SuperArgus family of scanners (Wang *et al* 2006). It features six detector modules arranged in a single ring, resulting in three pairs of detectors at 180°. Each module consists of 338 pixels, arranged in a 13 × 13 crystal matrix, with a crystal pitch of 1.55 mm and a reflector thickness of 0.1 mm. The maximum imaging field of view (FOV) has a diameter of 60 mm and 20 mm in height. The dual-layer phosphor sandwich (phoswich) enables depth of interaction capabilities, with a front layer of Lutetium Yttrium Orthosilicate (7 mm length) combined with an inner layer of cerium-doped gadolinium orthosilicate (8 mm length). The light output of the phoswich is coupled to position-sensitive photomultiplier tubes (PMTs).

The PMT signals are fed into a custom-made, real-time, FPGA-based digital data acquisition system. Signals from the six detectors are distributed across two FPGA boards. An Ethernet interface based on the User Datagram Protocol is employed for real-time data transfer at 2 × 1 Gbit s^{-1}, 1 Gbit s^{-1} interface per each FGPA. With this configuration, aggregated maximum transfer rates to the personal computer (PC) of 6 million counts per second (Mcps) singles per FPGA (2 Mcps for detector) can be sustained continuously, comparable to the highest maximum rates of existing commercial PET systems. At the detector level, events are acquired and grouped into packets of ∼80 singles, stored temporarily in the buffer of each FPGA, previously to being sent to the Ethernet interfaces. This approach serializes the Poisson nature of acquisition, mitigating dead-time and avoiding Ethernet bottlenecks, taking advantage of the period during accelerator pulses for data transmission. Peak rates at each detector can reach 5 Mcps with acceptable dead-time, for the system considered.

In our actual application, the detector provides the spatial position (pixel of interaction in the detector array), energy and timestamp for each single-event acquired. Timestamps with 156.25 ps binning are stored. Coincidences are sorted in the PC based on the timestamps of each event. An in-house developed digital sorting algorithm sorts single events in chronological order, grouping them into small batches of hundreds of events to establish coincidences within a given time window. The algorithm is designed for real-time implementation, allowing quasi-instantaneous output of sorted coincidences after as low as 128 ms buffering of data.

2.2. Experiment

The experiment was conducted at the Quirónsalud PT center in Madrid, Spain. The facility is equipped with a clinical Proteus-ONE system by IBA. This system consists of a compact synchrocyclotron (S2C2) that delivers proton beams with energies up to 230 MeV to a single treatment room equipped with a 220° gantry. The internal RF frequency in the 60–90 MHz range and pulses of 10 μs width are provided with a repetition rate of 1 kHz (Garcia-Diez *et al* 2023).

Homogeneous cylindrical PMMA phantoms ($C_5H_8O_2$, with density of 1.19 g cm^{-3}) of dimensions 50 mm in diameter and 50 mm in height, were fixed in a custom-made 3D printed phantom holder placed in the center of the FOV, positioned 10 mm away from the bottom of the scanner FOV. Before irradiation, the phantom was aligned with the gantry isocenter using the laser positioning system. Irradiations were performed using a single 70 MeV proton pencil beam delivering 70 monitor units (MU) in less than 5 s. It corresponds to a physical dose of 2 Gy at the entrance and 8.4 Gy at the Bragg peak maximum. This dose distribution is displayed in figure 1. The treatment plan was created using the RayStation 2024A (RaySearch

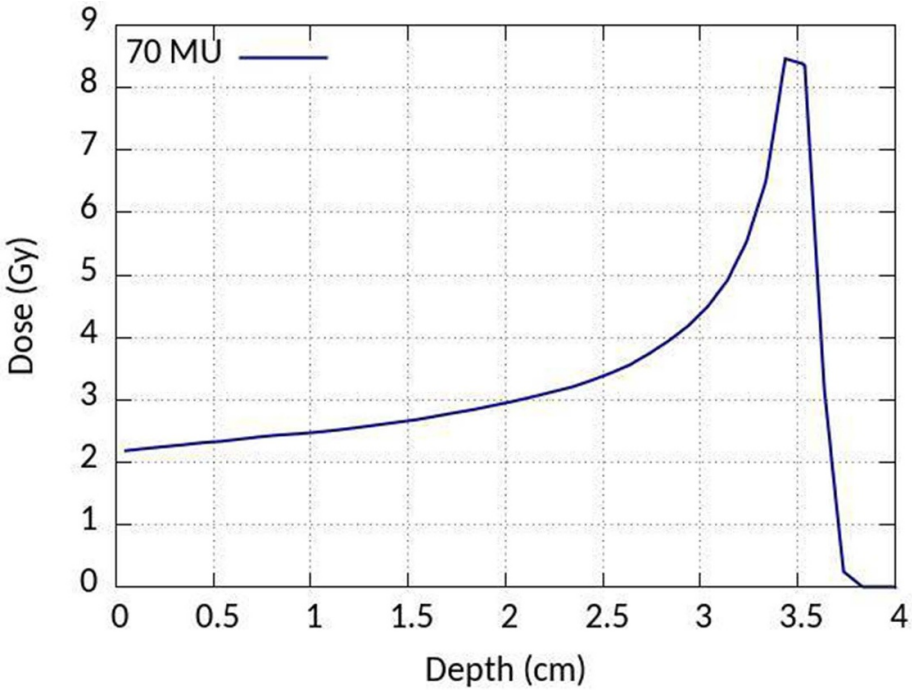

Figure 1. Longitudinal dose profile (integrated over the lateral dimension) calculated with the RayStation 2024A TPS for a 70 MU proton irradiation in the PMMA phantom.

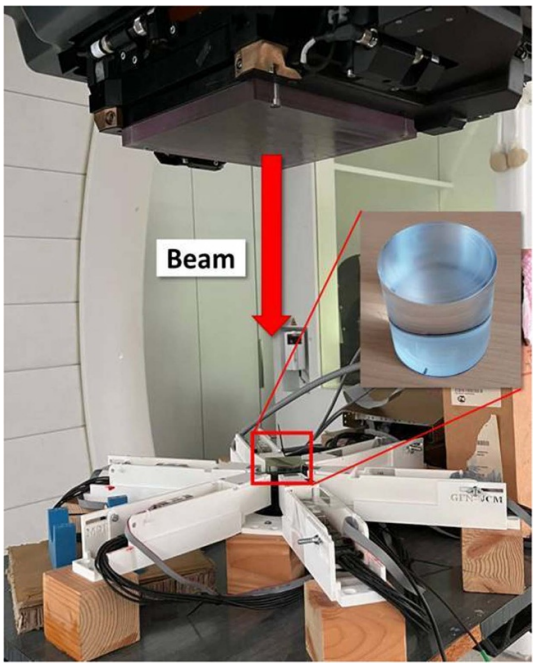

Figure 2. Photo of the experimental setup employed during the irradiation of the PMMA phantoms.

Laboratories AB, Stockholm, Sweden) treatment planning system (TPS). The beam was perpendicular to the axial plane of the scanner (see figure 2).

For each measurement, data acquisition spanned approximately 400 s, encompassing pre-irradiation, beam-on, and post-irradiation periods (∼60 s pre-irradiation. + 5 s beam-on + ∼300 s post-irradiation).

2.3. Online activity reconstruction

List mode data (LMD) files were directly stored in a host PC. Image reconstruction was performed on the PC using a MLEM algorithm. To meet the demands of online imaging, the MLEM algorithm was implemented on a GPU architecture for efficient and fast processing. For the experiment, the code was tailored to read the

LMD files and reconstruct 3D images using a continuous data stream without reverting to the first event upon reaching the end of the list file.

For this experiment, data was acquired throughout the whole irradiation period, including both in-spill and inter-spill events. Coincidences were processed with a 450–650 keV energy window and a 10 ns time window and considering data from the two phases. During the measurements, both coincidence sorting and image reconstruction algorithms simultaneously access the list file where coincidences are being stored. This synchronization is achieved through optimized shell-script parallelization, with list data temporarily held in a first-in-first-out memory area to enable interprocess communication. The code reads an external user-defined input file to specify update and reset times for PET image reconstruction. Images were reconstructed using 5 MLEM iterations. With this approach, 3D PET activity maps are reconstructed on-the-fly in less than one second.

2.4. In-beam dose estimates

3D dose maps were reconstructed from the measured in-beam PET data using the DAD-MSA algorithm proposed by Onecha *et al* (2022). The method uses a precomputed database containing the ideal PET images that ^{15}O, ^{13}N and ^{11}C would generate independently for each pencil beam in the treatment plan. The DAD-MSA then adapts the database to specific scenarios by combining the contributions of each isotope, based on the initial and final time of the measurements, as well as the length of the beam-on period. To reconstruct the dose, the measured activation image is used as input, and the DAD-MSA algorithm searches for the optimal linear combination of precomputed PET activities in the DAD that best fits the input. This enables dose estimation in under 0.5 s.

In this study, the dictionary was calculated from a simulated PT plan involving irradiation of the full PMMA phantom. The plan consisted of 625 pencil beams with energies ranging from 50 to 80 MeV, divided into 25 energy layers. Each layer was further subdivided into a grid of 25 equally spaced beams, separated by 5 mm in the X and Y directions. The position of each beam was modeled using a Gaussian spatial distribution ($\sigma = 0.55$ mm). All simulations were conducted using the TOPAS-MC tool (Perl *et al* 2012), from which both activity and dose data were obtained. The dimensions of the scorers were set to match the FOV of the MiniPET scanner, ensuring alignment with the reconstructed PET images.

2.5. IDE-PET

The IDE-PET is a novel tool developed in this study, integrating the aforementioned methodology for activity and dose reconstruction, enabling real-time visualization during and immediately after irradiation. The main program and all subroutines are written in the FORTRAN77 programming language combined with NVIDIA CUDA and PGI CUDA Fortran Compilers.

Figure 3 illustrates a simplified IDE-PET workflow. The routines for activity and dose reconstruction operate in a pipelined fashion, with each routine forwarding its output to the next one. First, a PET image is generated based on the measured data accumulated within the time interval specified in the user-defined input parameters file. This activity map is then displayed and sent to the DAD-MSA algorithm, which computes the deposited dose considering the contribution of each isotope using the live-time of the measurement. Although post-irradiation live-time is accounted for, this does not provide a significant advantage, as the contribution of ^{15}O remains dominant during the first few minutes (>90%).

The dose is displayed online and used to calculate the proton range. This process runs continuously throughout the entire acquisition period. The IDE-PET tool features a graphical user interface (GUI) that displays PET activity and corresponding dose on the host computer.

3. Experimental procedures

Potential and limitations derived from the integration of the IDE-PET tool and the MiniPET in-beam scanner are investigated in detail. For this purpose, three different aspects of the experimental setup combined with IDE-PET have been studied in order to assess its applicability for online PT monitoring.

3.1. Study of the MiniPET performance for in-beam applications

The modular nature of the MiniPET system provides flexibility for in-beam applications, being able to handle a different number of detectors and enabling measurements in several configurations. The open-ring geometry (figure 4(a)) features a gap in the center of the ring, allowing irradiations with the beam crossing the scanner. The use of PET scanners with an open configuration has been proposed for in-beam applications (Parodi *et al* 2023) since they provide substantial advantages compared to closed configurations due to their ease of integration into the treatment room, albeit at the expense of reduced resolution along the

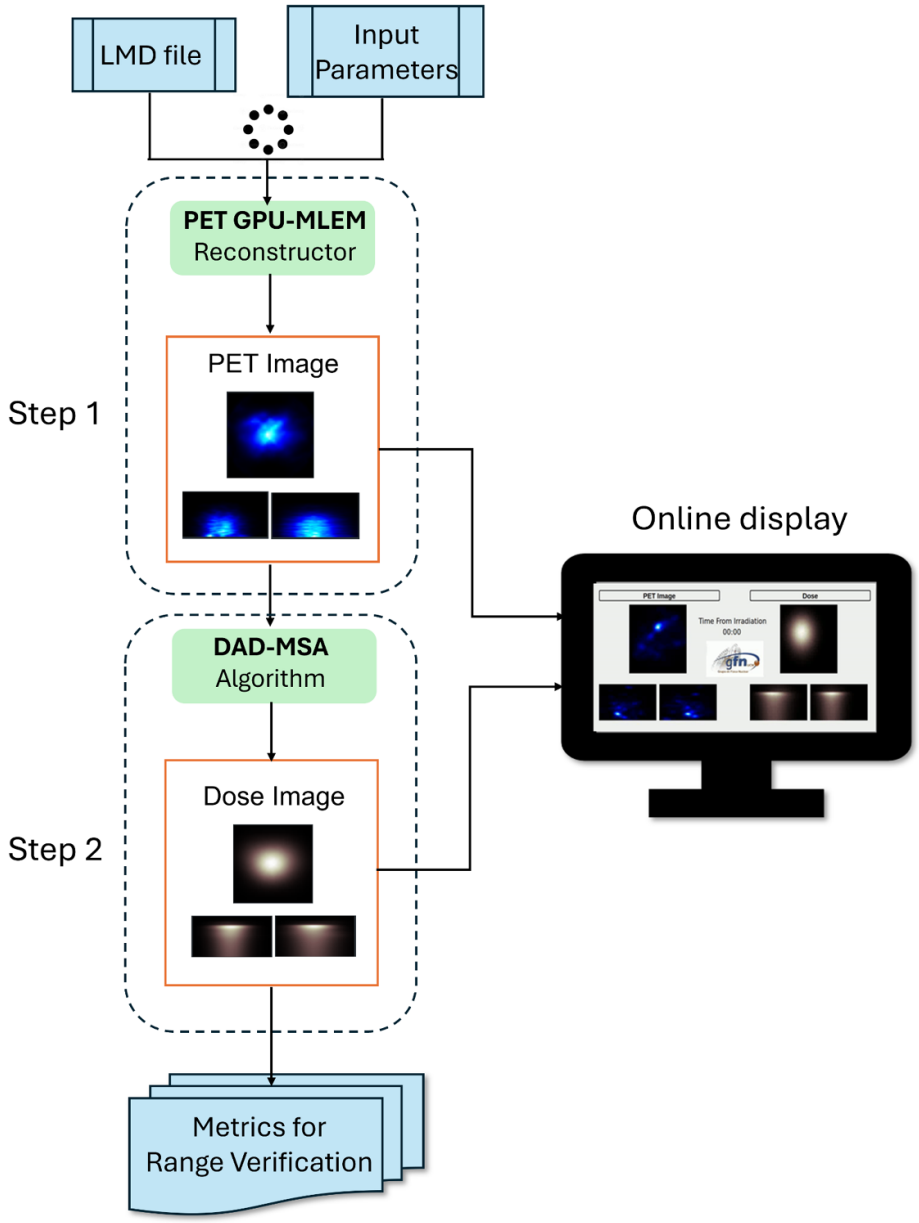

Figure 3. Schematic representation of the IDE-PET workflow designed for online activity and dose reconstruction.

aperture direction. The gapless closed-ring geometry (figure 4(b)) is less prone to artifacts compared to the open one but is only suitable for irradiations where the scanner is perpendicular to the beam direction.

An in-beam experiment was conducted using the open-ring configuration with the beam positioned perpendicular to the scanner (similar to the setup shown in figure 2) to study the influence of this geometry in the quality of the PET images. The FOV of the reconstructed image is $40 \times 40 \times 20$ mm^3, with a $0.5 \times 0.5 \times 0.5$ mm^3 voxel size. For the closed-ring geometry, the FOV of the reconstructed image is $50 \times 50 \times 20$ mm^3, with a $0.625 \times 0.625 \times 0.5$ mm^3 voxel size.

3.2. Range shift verification accuracy

The next step focuses on evaluating the accuracy of the proposed method for range shift prediction. To investigate this, five different PMMA range shifter foils with varying thicknesses of 1.0, 1.5, 2.0, 3.0, and 5.0 millimeters were placed at the proximal surface of the phantoms to change the depth of the proton beam. The closed-ring configuration of the MiniPET scanner was employed for this study due to its superior angular coverage and fewer imaging artifacts.

Following the methodology described in (Onecha *et al* 2022), we define a set of metrics to compare the reconstructed dose of the shifted measurements against the reconstructed dose with no range shifter, which is considered as the reference or ground truth dose. Range deviation histograms have been obtained from the

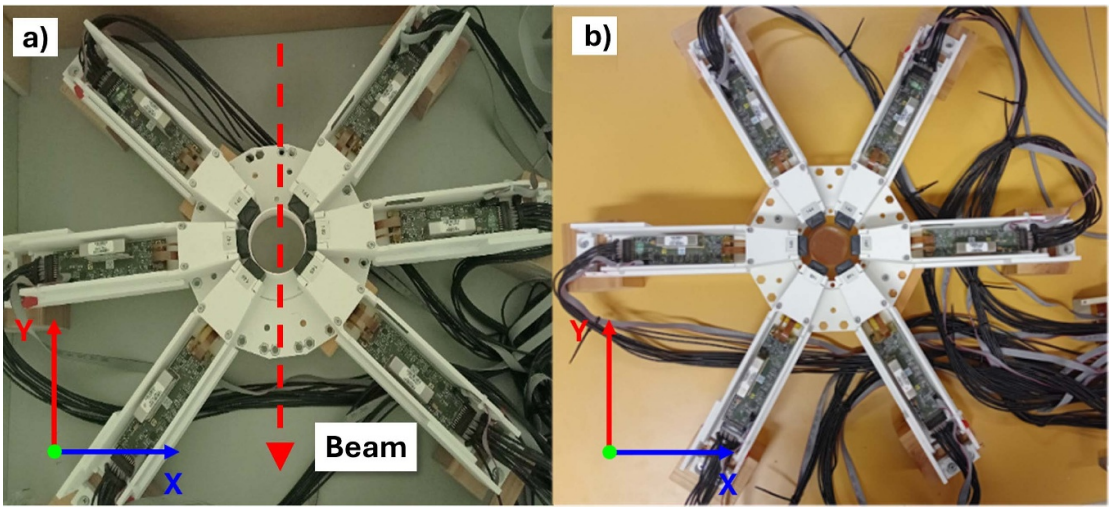

Figure 4. The MiniPET scanner features a single ring comprising six detectors. Two configurations are proposed for proton-beam irradiation: (a) open-ring and (b) closed-ring.

corresponding dose map distributions. Then, at every voxel in the transverse XY plane, including non-zero voxels along the beam propagation direction, the percentage depth dose (PDD) at the 50% and 90% positions (R_{50} and R_{90}) have been computed. The R_{50} and R_{90} values represent the z-coordinates along the longitudinal dose profile at which the dose reaches 50% and 90% of its maximum at the Bragg peak.

The differences between R_{50} and R_{90} of the shifted measurements and the ground truth are defined as ΔR_{50} and ΔR_{90} values, respectively. These metrics serve to evaluate our system's accuracy in predicting range shifts, as they quantify range deviations relative to the planned dose and its associated error, identified as the mean and sigma values of these range deviation histogram distributions.

3.3. Limit of range deviation detectability

Finally, we aim at investigating the limitations of the proposed method to detect range shifts in terms of the minimum proton dose and the maximum elapsed time after treatment completion. We use these two variables since they are critical parameters for online monitoring in PT. The delivered dose should not exceed the typical clinical dose per field, which ranges between 1 and 2 Gy at the Bragg peak. In addition, feedback on the treatment should be available with minimum delay, compatible with real-time monitoring, to minimize washout effects (Grogg *et al* 2015) and allow for prompt interruption in case of erroneous dose delivery.

Firstly, to investigate the impact of the dose on the range shift estimation, new datasets were generated by randomly sampling PET events from the original 70 MU measurement yielding irradiations of 30, 20, 10, 5 and 1 MU. Next, PET images and dose distributions for every sample within these new datasets were reconstructed at different points from the start of irradiation, spanning 60 s (5 s of irradiation followed by 55 s of decay). The corresponding range shifts with respect to the ground truth scenario were calculated at different times for the R_{50} PDD values, enabling the determination of the optimal dose-time scenario for range shift prediction.

3.4. Uncertainty analysis

In the previous work of Onecha *et al* (2022), only relative errors were reported as the differences between the reconstructed and the planned dose maps for the R_{50} and R_{90} estimates, which provide information on the accuracy of the method.

In the present work we aim to extend this approach to give the total uncertainty associated with the range prediction as a function of dose and elapsed time by calculating the corresponding error. To this end, 100 additional quasi-independent samples were generated for the MU values outlined earlier, employing different random seeds. This provides a measure of the precision of the method. After reconstructing the dose maps for these samples at different time points, the total uncertainty for the R_{50} proton range, here denoted as $\delta R_{50,\mathrm{MU,dt}}$, was determined considering both statistical (standard deviation across samples) and absolute (deviation from a reference value) errors, using the following equation:

$$\delta R_{50,\,\mathrm{MU},\,\mathrm{dt}} = \sqrt{\sigma^2_{\mathrm{MU},\,\mathrm{dt}} + \left(R^{\mathrm{ref}}_{50} - R^{\mathrm{obs}}_{50,\,\mathrm{MU},\,\mathrm{dt}}\right)^2} \tag{1}$$

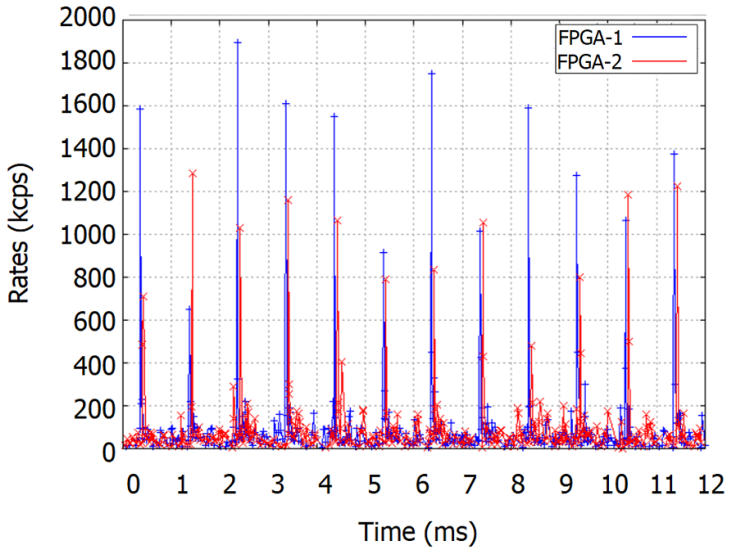

Figure 5. Single events as a function of time measured in each FPGA (3 detectors) during the beam-on period. The characteristic pulsed time structure (10^{-3} s) of the IBA Proteus One is seen. During the acquisition all single events (in-spill and inter-spill) are collected.

where $\sigma_{\mathrm{MU,\,dt}}$ represents the standard deviation obtained from the distribution of the 100 reconstructed samples, R_{50}^{ref} is the chosen reference PDD value from the measurement at 70 MU reconstructed with the full acquisition from the start of the irradiation (240 s), and $R_{50,\,\mathrm{MU,\,dt}}^{\mathrm{obs}}$ is the mean PDD value obtained from the reconstructed dose maps of the sampled datasets. The subscripts MU and dt are used here to indicate the number of MU of the dataset considered and total acquisition time from the start of the irradiation employed to reconstruct the dose and extract the corresponding $R_{50,\,\mathrm{MU,\,dt}}^{\mathrm{obs}}$ value. This approach allows the evaluation of both the precision and accuracy of the proposed method for dose reconstruction.

4. Results

4.1. Performance for in-beam measurements

Figure 5 shows the rate of single events per FPGA board (each processing events from three detectors) as a function of time, for a particular irradiation of PMMA over a 12 ms beam-on period. The pulsed time structure of the IBA Proteus One accelerator, characterized by 10 μs pulses delivered at 1 kHz (Garcia-Diez *et al* 2023), is evident, showing the timing capabilities of the system throughout irradiation. During the measurement, data is continuously saved in list mode, including in-spill and inter-spill events, which are stored for subsequent analysis. About an 8-fold increase in the rates is observed during the spill phase due to the prompt radiation from photons, charged particles, and neutrons. We achieved maximum instantaneous rates of up to 8 Mcps, without significant losses or issues with electronic parallelization, maintaining a high detector performance during in-beam beam-on acquisition.

Projected 2D PET images reconstructed using the open and closed-ring geometries of the scanner for irradiation in the nominal configuration (no range shifter) of a PMMA phantom are presented in figure 6 for comparison. The open-ring configuration enables directing the beam through the center of the PET system but results in reduced geometric coverage, leading to image quality degradation and causing a significant artifact in the transverse plane of the scanner, due to the gaps between the three pairs of detectors. The closed-ring configuration was selected for further experiments.

4.2. Online dose maps using IDE-PET

Figure 7 shows an example of the GUI of the IDE-PET tool from the nominal irradiation at 70 MeV with the closed-ring configuration, 29 s after the start of the irradiation. The GPU-based activity reconstructor takes approximately 0.2 s to generate the PET image (left panel), while the DAD-MSA requires approximately 0.5 s to output the corresponding dose (right panel). In this case, both quantities are updated every second, based on the coincidences measured within that time frame, falling in a 450–650 keV energy window. They are presented in three different projections for each Cartesian plane to enable 3D visualization. At any time, the user can select the frame time for PET and dose visualization, as well as the reset time for initializing the processed coincidences.

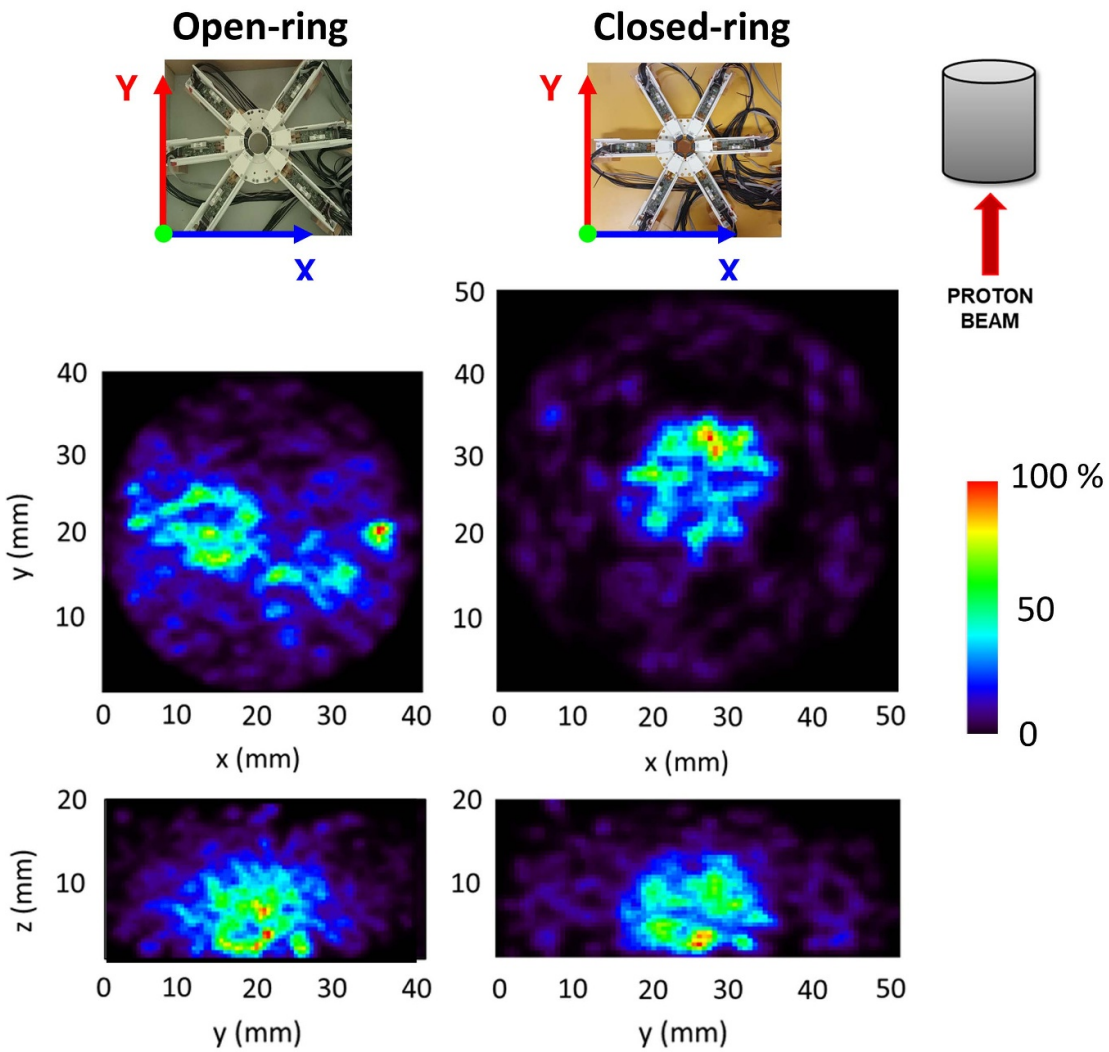

Figure 6. 2D reconstructed PET images (summed along the perpendicular coordinate) from the measurement of a pencil beam irradiation at 70 MeV, acquired using the open-ring (left) and closed-ring (right) geometries of the MiniPET scanner.

Figure 7. GUI of the IDE-PET tool, illustrating the measured in-beam activity (left) and the dose calculated using the DAD-MSA algorithm (right) following irradiation with a 70 MeV proton beam on a PMMA cylinder 50 mm in height and 50 mm in diameter. Both quantities are displayed at 29 s after the start of the irradiation. During this time period, data is updated in 1 s time frames, with coincidences progressively accumulated from the beginning of the irradiation.

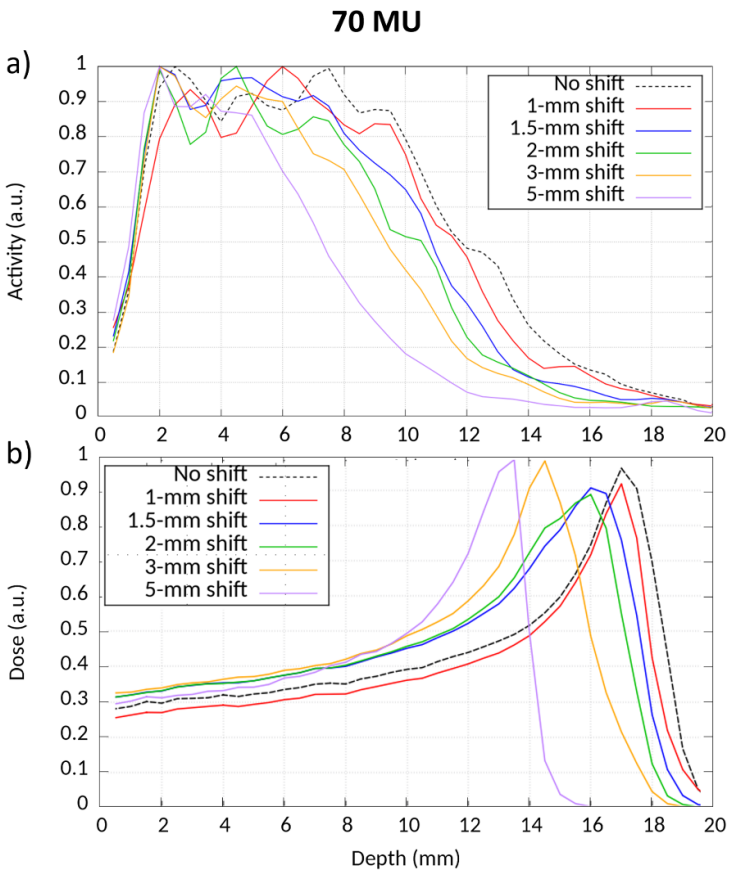

Figure 8. Projected 1D activity (a) and dose (b) profiles along the beam direction, obtained from the measurements of a 70 MeV proton beam in a 50 mm in diameter and 50 mm in height cylindrical PMMA phantom with 70 MU and PMMA range shifters of different thicknesses. Profiles were determined over 60 s from the start of the irradiation.

A video showing the activity and dose distributions in the phantom during the first minute is included as supplementary material to provide a visual representation consistent with the experimental observations.

4.3. Range deviation identification

Figures 8(a) and (b) show the 1D activity and corresponding dose profiles, summed in the lateral direction within the PMMA phantoms for the measurements with different range shifters. The nominal configuration is also included. The results are displayed along the beam direction in the phantom. In all cases, profiles were determined by accumulating data for the first 60 s from the beginning of the irradiation and including both in-spill and inter-spill events in the beam-on period. As expected, the introduction of range shifts induces an upstream displacement of the activity and dose profiles relative to the nominal configuration.

Figures 9(a) and (b) show the ΔR_{90} and ΔR_{50} range deviation histograms for measurements with range shifters, relative to the nominal configuration. These histograms are generated by analyzing the 3D dose matrix along the beam direction (Z). Specifically, for each point in the transverse (X,Y) plane, the corresponding column of pixels along the Z-axis is extracted. If the resulting dose profile is significant compared to the maximum dose, the range is calculated and compared to the reference distribution at the same (X,Y) location. The final histogram includes all these points, with the mean value representing the overall deviation and the sigma providing insight into the spatial accuracy of the reconstruction. Less dispersed values and a closer match to the expected range shift indicate a more accurate range shift prediction.

Mean and sigma values obtained from the ΔR_{90} and ΔR_{50} range deviation histograms shown in figure 9 are listed in table 1, together with the corresponding experimental induced range shifts. Here, the mean value is considered the predicted range deviation. For a 70 MU dose fraction, the ΔR_{90} or ΔR_{50} obtained from the reconstructed doses are sensitive to every induced range shift, even to the 1 mm smallest deviation.

4.4. Sensitivity to acquisition time and dose

Figure 10 presents the evolution of the ΔR_{50} as a function of the time, computed every second from the beginning of the irradiation. The measurement with the 3 mm range-shifter is taken as a case study for the

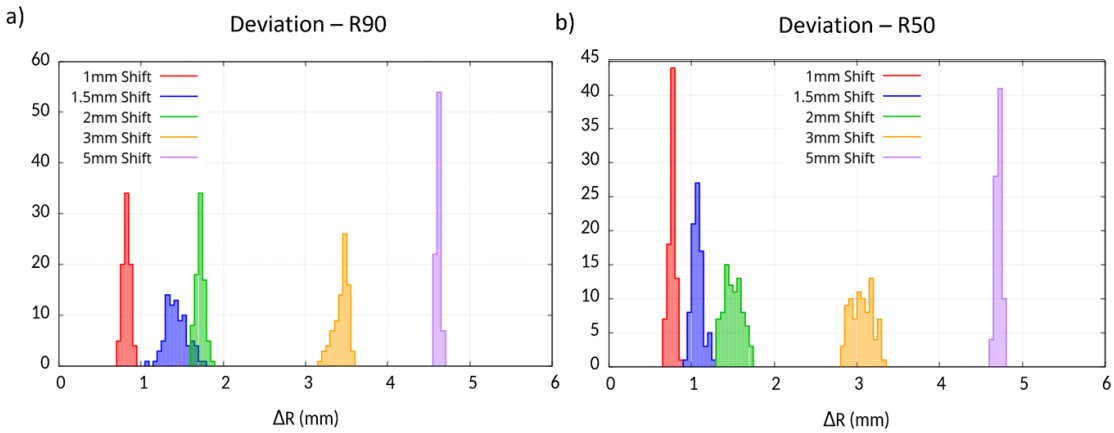

Figure 9. Histograms of range deviations derived by contrasting the R_{90} (a) and R_{50} (b) values of the various shifted measurements and the ground truth measurement with no range shift.

Table 1. Mean and sigma values obtained from the range deviations histograms of figure 9 for different range shifter widths.

Range shifter width (mm)	Induced range shift (mm)	ΔR_{90} (mm)		ΔR_{50} (mm)	
		Mean	Sigma	Mean	Sigma
1.00	0.82	0.80	0.05	0.74	0.04
1.50	1.31	1.41	0.13	1.05	0.07
2.00	1.75	1.70	0.05	1.48	0.11
3.00	2.61	3.02	0.09	2.78	0.13
5.00	4.48	4.59	0.03	4.68	0.04

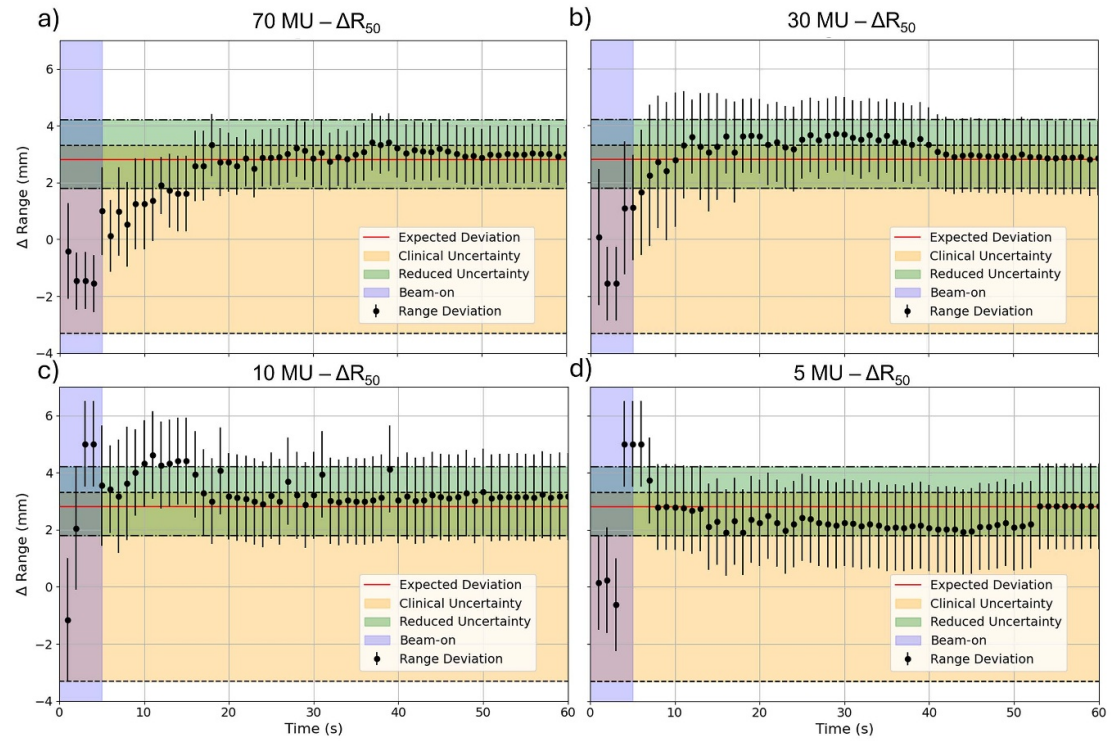

Figure 10. Evolution of the ΔR_{50} range shift prediction as a function of acquisition time for different dose levels (a) 70 MU, (b) 30 MU, (c) 10 MU and (d) 5 MU in the 3 mm range shifter scenario. The origin ($t = 0$) of the time axis corresponds to the start of the beam-on period.

analysis. The x-axis spans the first 60 s and during this time coincidences are progressively accumulated to generate the PET image and subsequent dose reconstruction with IDE-PET. This offers insight into the minimum elapsed time required to accurately identify inconsistencies in the planned treatment. Similarly,

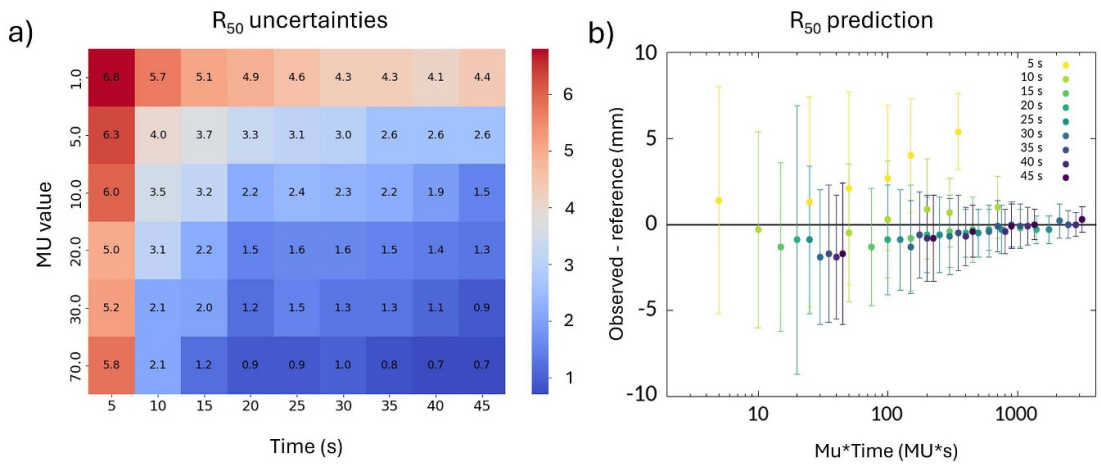

Figure 11. (a) 2D heatmap showing the progression of the total uncertainty (relative plus statistical) with increasing acquisition time and MU for the R_{50} values. (b) Combined effect of MU and time on the accuracy of the R_{50} prediction relative to the reference value at 70 MU with the full acquisition. Error bars correspond to the total uncertainties presented in (a).

the same evaluation has been performed over different MUs down to 5 MU, extrapolated from the original irradiation at 70 MU, to determine the dose sensitivity of the online monitoring. This lower limit was set for the study because a significant loss of precision in the range shift prediction was observed in Onecha *et al* (2022) for a 0.1 Gy dose fraction. Each data point is accompanied by an error bar, resulting from the standard deviation (sigma) of the range deviation histograms.

Furthermore, to demonstrate the clinical significance of these results, two uncertainty bands are also included in the figures. The reduced uncertainty represents an accuracy of $\pm$1.2 mm or less in the range shift prediction and is plotted in green. The clinical uncertainty band reflects current uncertainty guidelines, which typically set a 3.5% of the proton range plus 2 mm (Paganetti 2012), giving a $\pm$3.5 mm error band, plotted in light orange.

In the first seconds, the lack of statistics leads to poor range shift prediction, as expected. At 70 MU, the range shift prediction progressively improves while accumulating statistics, converging to the expected deviation within approximately 20 s. No further improvement is seen with increased acquisition time beyond this point. A similar trend is observed for the analysis of the synthetic data sets at 30 and 10 MU. However, in these cases, the range shift prediction is less accurate, showing increased variability around the expected value. At 5 MU, the convergence is slower, and approximately 50 s are necessary to obtain an accurate range shift prediction.

4.5. Total uncertainty in the range shift estimation

Figure 11(a) represents a heatmap isolating the total uncertainty of R_{50} values calculated using equation (1) as a function of reconstruction time and delivered MU. An extra row is included showing the uncertainties computed at 1 MU. Total uncertainties range from approximately 0.7–6.8 mm, with the minimum and maximum located at the extremes of the dose-time tuples considered.

A clear effect of the dose and acquisition time can be inferred from this visual representation. As either decrease, uncertainties increase. This MU/time effect ultimately comes down to the number of PET coincidences, since more counts result in lower statistical uncertainty. At lower MU values (e.g. 1.0 MU and 5.0 MU), uncertainties remain relatively high even with longer acquisition times. However, at higher MU values (10 MU or larger), the uncertainties drop significantly within the first 10–15 s and stabilize below 2 mm after 20 s, meeting current clinical guidelines.

Figure 11(b) summarizes this information in a scatter plot, showing differences between observed and reference (70 MU and full acquisition time) R_{50} values as a function of the dose-time product. Error bars reflect the total uncertainties from figure 11(a). Positive outliers are observed for the doses reconstructed using the first five seconds. As acquisition time increases, differences between observed and reference values diminish converging to nearly zero, indicating accurate R_{50} reconstruction relative to the reference value.

5. Discussion

The feasibility of simultaneous online activity and dose reconstruction from experimental in-beam PET data has been demonstrated in this work, by means of a new MiniPET in-beam system, a custom-made modular

PET scanner. To the best of our knowledge, this is the first time both capabilities are realized in real time. We take advantage of the operation in a high-detection regime, enabling beam-on imaging, where the system is able to sustain maximum instantaneous count rates of approximately 2 Mcps per detector while maintaining both good spatial and temporal resolution. The integrated IDE-PET tool makes it possible to reconstruct both the PET activity and the dose, enabling the reconstruction of 3D activation images in less than one second from the start of the beam-on period.

5.1. Online activity reconstruction

In contrast, most proposed in-beam PET scanners described in the literature lack the capability to provide real-time information of the activation during the time the beam is on. Clinical trials performed with the GSI (Enghardt *et al* 2004a) and with the BOLPs-RGp in-beam PET systems (Nishio *et al* 2010) reported treatment feedback within 1 h and 200 s after proton beam irradiation, respectively, which makes potential changes in treatment plans only possible for the ensuing treatment fraction. The J-PET scanner (Shopa *et al* 2021) is designed with a dedicated FPGA system-on-chip platform which could potentially enable real-time image reconstruction, but it has not been experimentally tested yet. The INSIDE in-beam PET scanner (Ferrero *et al* 2018) is the only other in-beam PET system that has demonstrated dynamic reconstruction capabilities. However, its time resolution of 10 s may be inadequate for real-time treatment feedback. Using MiniPET and IDE-PET we are capable of producing activation maps in less than a second after the start of the irradiation.

5.2. Online dose reconstruction

Regarding dose reconstruction, several methods have been proposed in literature, but the filtering approach is the only one that has been experimentally validated (Hofmann *et al* 2019, Masuda *et al* 2019, 2020). However, this method lacks real-time implementation and requires several minutes to estimate a 1D dose profile from data collected over half an hour (Hofmann *et al* 2019). A MLEM implementation has demonstrated improved dose reconstruction capabilities (Masuda *et al* 2019). For a 2 Gy fraction, the method proved able to reconstruct the 2D dose distribution of a homogeneous PMMA phantom, irradiated with a single beam and also a Spread-Out Bragg Peak (SOBP). Nonetheless, results were available 200 s post-irradiation with a relative error within 10%, which is considerably higher than the relative error obtained in this work at 10 s post-irradiation for the same dose. A more recent work extended the analysis to an inhomogeneous target, calculating 3D dose distributions via Monte Carlo simulations with similar relative errors (Masuda *et al* 2020). However, 30 s were required to estimate the dose, which was available 200 s after irradiation.

In-silico studies using deep learning approaches have demonstrated promising results in reconstructing the dose from simulated in-beam PET data (Liu *et al* 2019, Hu *et al* 2020, Ma *et al* 2020, Rahman *et al* 2022). Although the trained neural network model can output the dose distribution in milliseconds, these models still require long acquisition times of 300 (Rahman *et al* 2022) or 600 s (Hu *et al* 2020, Ma *et al* 2020) to estimate the dose, when considering a 2 Gy dose fraction. For a monoenergetic beam, this framework can predict the dose distribution with relative errors within 1% and a range uncertainty of 0.3 mm using an open-ring 220 modules PET scanner (Hu *et al* 2020). When the scanner is reduced to a 8-module prototype, relative deviations within 1%–2% can still be achieved, together with a shift in BP below 1 mm (Rahman *et al* 2022), which are still comparable to the sensitivity and precision presented in this work.

In our system we propose a method that uses a DAD generated through MC simulations to reconstruct 3D dose maps from PET images with enhanced accuracy and real-time performance. This method decouples time-intensive simulation steps from the reconstruction phase by precomputing dose and activation maps for every proton pencil beam in a treatment plan. The DAD is integrated with a MLEM and MSA algorithm, allowing for rapid, intra-fractional dose verification by identifying the optimal linear combination of precomputed activity maps to match observed PET data. Through this approach, the corresponding dose distributions can be obtained every second.

5.3. Range verification performance

Due to the absence of experimentally implemented dose reconstruction algorithms, experimental trials using in-beam PET systems described have primarily focused on detecting changes within the activity profile of reconstructed PET images for range verification. This approach enables the possibility of performing intra-fraction range verification. Notably, a recent study has demonstrated the feasibility of achieving an accuracy and precision of 0.6 ± 0.3 mm within 60 s for a $\sim$0.5 Gy dose fraction using a prototype human brain PET system (Yang *et al* 2024). Regarding clinical trials, the first and largest patient cohort, performed with carbon ions at the GSI, reported that the in-beam PET system could detect range deviations of about 5 mm, in line with the limited spatial resolution of the detectors (Enghardt *et al* 2004b). A smaller study, with a 48-patient sample, also reported an excess of 2 mm in the activity resolution during treatment with protons

(Nishio *et al* 2010). The INSIDE PET system has demonstrated better results, bringing an average standard deviation of approximately 2.5 mm in six patients without morphological changes (Moglioni *et al* 2022). For clinical studies with in-room or offline PET systems, accuracies between 1–5 mm have been reported. Additionally, a simulation study using a 95 patient sample has been recently conducted with the J-PET scanner, yielding a promising submillimeter precision of 0.23 mm (Brzeziński *et al* 2023).

In this work, a quantitative analysis has been performed to determine the impact of reducing the dose and acquisition time on range estimation, as these are the primary and most controllable parameters affecting range monitoring in PT. Statistical significance is reached within 20 s from the start of the irradiation, with differences between the expected and calculated range shifts below 1 mm, close to the spatial resolution of the PET scanner. This is valid for beam intensities down to 5 MU, equivalent to a dose of 0.6 Gy at the Bragg peak maximum. The low dose and short time would potentially enable intra-beam range verification and the detection of treatment deviations during delivery, allowing the partial adaptation of the beam before the next field. As discussed earlier, the present treatment planning uncertainties are defined as 3.5% of the proton range plus 1–3 mm depending on the center (Paganetti 2012). For a 70 MeV proton beam this results in a range uncertainty of about 3.5 mm.

It is also important to note that in this study, beam-on periods have been kept constant across all cases. In clinical practice, however, a reduced MU results in shorter irradiation times. Given the duration of the beam-on period and the half-lives of the isotopes considered, variations in irradiation time or beam intensity have minimal impact on the results. Nevertheless, this effect should be carefully evaluated when considering different isotopes or significantly longer irradiation times.

5.4. Total uncertainty in the range prediction

Additionally, we have conducted a detailed analysis of the total prediction uncertainty, computing relative and statistical errors for the R_{50} proton range values, using a sample of sub-datasets obtained from the original measurement. The sensitivity analysis indicates that both the acquisition time and dose have a meaningful impact on the total uncertainty. A pivotal finding for our approach is that after 20 s, the total uncertainty determined drops below 2 mm, for a 10 MU dose (equivalent to about 1 Gy). This promising technology should help reduce clinical uncertainties. However, it should be noted that range uncertainty in a clinical scenario is related to uncertainty in biological tissue, which is not the focus of the current experiment. Therefore, further development and research will be needed.

5.5. Limitations

A number of potential improvements of the present work must be stressed. First, all events acquired during the irradiation period have been considered for the activity (and dose) reconstruction. At synchrotron and cyclotron-based facilities, data processing algorithms have been successfully implemented to make use of the beam time structure (Kostara *et al* 2019, Gao *et al* 2020), to take advantage of the lower background during the off-spill periods, which are of the order of seconds. This is not so straightforward in superconducting synchrocyclotrons, such as the one employed in this work, where the beam is pulsed with a frequency of about 1 kHz, with pulses lasting only a few microseconds (Garcia-Diez *et al* 2023). Here, a more sophisticated algorithm is required to filter out the prompt events emitted in this shorter period. Since our detection system is able to reconstruct the pulsed structure of the clinical beam whereby the true coincidence events can be selected, a coincidence discriminator for the acquired PET data will be implemented, and its impact on the resulting range prediction capabilities will be evaluated.

Second, all irradiations were conducted in a homogeneous phantom, limiting the current validation of range prediction to this straightforward scenario. To achieve a more thorough assessment, and move closer to clinical conditions, it is necessary to test the method in more complex situations, such as the irradiation of anthropomorphic or heterogeneous phantoms, paving the way for its eventual *in vivo* validation. Additionally, the evaluated treatment plan herein considered involved a single pencil beam. In clinical practice, however, multiple layers and beams are delivered, including SOPB, and the spatial and temporal combination of these fields should also be evaluated. To address this, we are currently developing deep learning-based workflows within this methodology. The PT digital TWIN models for dose verification with PET relies on a GPU implementation of an easy-to-train model architecture. In-silico tests have demonstrated promising results, predicting deviations within a tenth of a millimeter (Cabrales *et al* 2025).

6. Conclusions

This study provides the first-ever demonstration of real-time dose reconstruction from experimental PET measurements, combining an in-house developed modular PET scanner and a GPU-based workflow, the IDE-PET tool, for IDE. The methodology was validated through phantom experiments with artificially

induced range shifts, demonstrating millimeter sensitivity and the ability to compute doses every second with a minimal 1 s delay. A quantitative analysis was performed to find the optimal dose-acquisition time scenario. After 20 s from the start of the irradiation, our approach is able to reconstruct low doses (∼1 Gy at the Bragg peak maximum) with high accuracy and a total uncertainty of 2 mm. Overall, our proof-of-principle study validates the potential of the IDE-PET tool and the modular MiniPET scanner for real-time monitoring in PT. Future work will focus on enhancing the robustness of the proposed methodology, bringing it closer to its *in vivo* validation and the exploration of deep learning-based workflows for dose verification. For eventual clinical viability, a more complex PET scanner, equipped with a greater number of detectors, could be implemented to further enhance efficiency and improve dose reconstruction capabilities within this methodology.

Data availability statement

The data cannot be made publicly available upon publication because no suitable repository exists for hosting data in this field of study. The data that support the findings of this study are available upon reasonable request from the authors.

Acknowledgments

This work was funded by Comunidad de Madrid, Spain under Projects PRONTO-CM (B2017/BMD-3888) and ASAP-CM (S2022/BMD7434). We acknowledge support by UCM under project pFLASH (PR27/21-014); Spanish MCIN/AEI/10.13039/501100011033 under Grants RADFLAP (PID2021-124094OA-I00), FLASHonCHIP (PLEC2022-009256), PROTOTWIN (TED2021-130592B-I00), mPET (PID2021-126998OB-I00) and INVENTOR (PID2022-137114OA-I00); European Union as part of the European Innovation Council's Pathfinder Open Programme: RETIMAGER, 101099096. The authors acknowledge the support from The Centro de protonterapia Quirónsalud, for the beam time, and its technical staff for their contribution to the operation of the accelerator. This contribution is for the Moncloa Campus of International Excellence, "Nuclear Physics Group-UCM," Ref. 910059. Part of the calculations for this work were performed on the "Computing Cluster for Physical Techniques," funded partially by UCM and partially by EU Regional Funds.

Conflict of interest

The authors declare no competing interests.

ORCID iDs

V V Onecha https://orcid.org/0000-0002-3531-2851
A Espinosa-Rodriguez https://orcid.org/0000-0001-9804-2900
C Soneira-Landín https://orcid.org/0009-0002-0760-4985
F Arias-Valcayo https://orcid.org/0000-0002-3814-0207
P Ibáñez https://orcid.org/0000-0001-8612-5303
S España https://orcid.org/0000-0001-9092-4597
D Sanchez-Parcerisa https://orcid.org/0000-0002-2245-9539
J A Vera-Sánchez https://orcid.org/0000-0002-3594-9457
A Mazal https://orcid.org/0000-0003-1391-8446
J M Udias https://orcid.org/0000-0003-3714-764X
L M Fraile https://orcid.org/0000-0002-6281-3635

References

Abouzahr F *et al* 2023 The first PET glimpse of a proton FLASH beam *Phys. Med. Biol.* **68** 125001
Arias-Valcayo F, Galve P, Herraiz J L, Vaquero J J, Desco M and Udías J M 2023 Reconstruction of multi-animal PET acquisitions with anisotropically variant PSF *Biomed. Phys. Eng. Express* **9** 065018
Bisogni M G, Camarlinghi N, Cerello P, Belcari N and Del Guerra A 2017 INSIDE in-beam positron emission tomography system for particle range monitoring in hadron therapy *J. Med. Imaging* **4** 011005
Brzeziński K *et al* 2023 Detection of range shifts in proton beam therapy using the J-PET scanner: a patient simulation study *Phys. Med. Biol.* **68** 145016
Cabrales P, Onecha V V, Izquierdo-García D, Fraile L M, Udías J M and Herraiz J L 2025 PROTOTWIN-PET: patient-specific deep learning models for 3D dose verification in proton therapy with PET *IEEE Trans. Radiat. Plasma Med. Sci.* 1–2
Camarlinghi N *et al* 2014 An in-beam PET system for monitoring ion-beam therapy: test on phantoms using clinical 62 MeV protons *J. Instrum.* **9** C04005

Crespo P, Shakirin G and Enghardt W 2006 On the detector arrangement for in-beam PET for hadron therapy monitoring *Phys. Med. Biol.* **51** 2143–56
Enghardt W, Crespo P, Fiedler F, Hinz R, Parodi J, Pawelke K and Pönisch F 2004a Charged hadron tumor therapy monitoring by means of PET *Nucl. Instrum. Methods Phys. Res.* A **525** 284–8
Enghardt W, Parodi K, Crespo P, Fiedler F, Pawelke J and Pönisch F 2004b Dose quantification from in-beam positron emission tomography *Radiother. Oncol.* **73** S96–S98
Espinosa-Rodriguez A *et al* 2024 SO052/#681—towards real-time submillimetric range verification from in-beam PET activation *Int. J. Part. Ther.* **12** 100364
Ferrero V, Camarlinghi N, Belcari N and Del Guerra A 2018 Online proton therapy monitoring: clinical test of a silicon-photodetector-based in-beam PET *Sci. Rep.* **8** 4100
Fourkal E, Fan J and Veltchev I 2009 Absolute dose reconstruction in proton therapy using PET imaging modality: feasibility study *Phys. Med. Biol.* **54** N217
Gao M *et al* 2020 First results from all-digital PET dual heads for in-beam beam-on proton therapy monitoring *IEEE Trans. Radiat. Plasma Med. Sci.* **5** 775–82
García Díez M, Espinosa Rodríguez A, Sánchez Tembleque V, Sánchez Parcerisa D, Valladolid Onecha V, Vera Sánchez J A, Mazal A, Fraile L M and Udias J M 2023 Measurement of the bunch structure of a clinical proton beam using a SiPM coupled to a plastic scintillator with an optical fiber *Med. Phys.* **50** 3184–90
Grogg K *et al* 2015 Mapping 15O production rate for proton therapy verification *Int. J. Radiat. Oncol. Biol. Phys.* **92** 453–9
Hofmann T *et al* 2019 Dose reconstruction from PET images in carbon ion therapy: a deconvolution approach *Phys. Med. Biol.* **64** 025011
Hu Z, Li G, Zhang X, Ye K, Lu J and Peng H 2020 A machine learning framework with anatomical prior for online dose verification using positron emitters and PET in proton therapy *Phys. Med. Biol.* **65** 185003
Ke L *et al* 2021 A real-time sorting algorithm for in-beam PET of heavy-ion cancer therapy device *Nucl. Eng. Technol.* **53** 3406–12
Kong J, Zhou X, Wang C, Chen J, Liang G, Du C, She Q, Qian Y and Yan J 2024 A dedicated in-beam PET system with a modular dual-head for radiotherapy imaging in HIMM *J. Instrum.* **19** 04021
Kostara E *et al* 2019 Particle beam microstructure reconstruction and coincidence discrimination in PET monitoring for hadron therapy *Phys. Med. Biol.* **64** 035001
Kraan A C, Hasegawa B H, Balter J M and Loo B W 2022 Localization of anatomical changes in patients during proton therapy with in-beam PET monitoring: a voxel-based morphometry approach exploiting Monte Carlo simulations *Med. Phys.* **49** 23–40
Liu C, Li Z, Hu W, Xing L and Peng H 2019 Range and dose verification in proton therapy using proton-induced positron emitters and recurrent neural networks (RNNs) *Phys. Med. Biol.* **64** 175009
Ma S, Hu Z, Ye K, Zhang X, Wang Y and Peng H 2020 Feasibility study of patient-specific dose verification in proton therapy utilizing positron emission tomography (PET) and generative adversarial network (GAN) *Med. Phys.* **47** 5194–208
Makkar S *et al* 2022 Image reconstruction using the PETITION PET scanner aimed at biologically guided proton therapy *Radiother. Oncol.* **170** S1386–S8
Masuda T, Nishio T, Kataoka J, Arimoto M, Sano A and Karasawa K 2019 ML-EM algorithm for dose estimation using PET in proton therapy *Phys. Med. Biol.* **64** 175011
Masuda T, Nishio T, Sano A and Karasawa K 2020 Extension of the ML-EM algorithm for dose estimation using PET in proton therapy: application to an inhomogeneous target *Phys. Med. Biol.* **65** 185001
Moglioni M *et al* 2022 *In vivo* range verification analysis with in-beam PET data for patients treated with proton therapy at CNAO *Front. Oncol.* **12** 929949
Montarou G, Lamare F and Santos R Chadelas R, Donnarieix D, Force P, Guicheney C, Insa C, Lambert D, Lestand L, Magne M 2017 Construction and tests of an in-beam PET-like demonstrator for hadrontherapy beam ballistic control *Nucl. Instrum. Methods Phys. Res.* A **845** 673–8
Nishio T, Miyatake A, Ogino T, Nakagawa K, Saijo N and Esumi H 2010 The development and clinical use of a beam ON-LINE PET system mounted on a rotating gantry port in proton therapy *Int. J. Radiat. Oncol. Biol. Phys.* **76** 277–86
Onecha V V, Galve P, Ibáñez P, Freijo C, Arias-Valcayo F, Sanchez-Parcerisa D, España S, Fraile L M and Udías J M 2022 Dictionary-based software for proton dose reconstruction and submillimetric range verification *Phys. Med. Biol.* **67** 045002
Paganetti H 2012 Range uncertainties in proton therapy and the role of Monte Carlo simulations *Phys. Med. Biol.* **57** R99
Parodi K *et al* 2007 Patient study of *in vivo* verification of beam delivery and range using positron emission tomography and computed tomography imaging after proton therapy *Int. J. Radiat. Oncol. Biol. Phys.* **68** 920–34
Parodi K and Bortfeld T 2006 A filtering approach based on Gaussian–power law convolutions for local PET verification of proton radiotherapy *Phys. Med. Biol.* **51** 1991–2005
Parodi K, Yamaya T and Moskal P 2023 Experience and new prospects of PET imaging for ion beam therapy monitoring *Z. Med. Phys.* **33** 22–34
Perl J, Shin J, Schümann J, Faddegon B and Paganetti H 2012 TOPAS: an innovative proton Monte Carlo platform for research and clinical applications *Med. Phys.* **39** 6818–37
Rahman A U, Nemallapudi M V, Chou C-Y, Lin C-H and Lee S-C 2022 Direct mapping from PET coincidence data to proton-dose and positron activity using a deep learning approach *Phys. Med. Biol.* **67** 185010
Remmele S, Hesser J, Paganetti H and Bortfeld T 2011 A deconvolution approach for PET-based dose reconstruction in proton radiotherapy *Phys. Med. Biol.* **56** 7601–15
Sanaat A, Amini M, Arabi H and Zaidi H 2024 The quest for multifunctional and dedicated PET instrumentation with irregular geometries *Ann. Nucl. Med.* **38** 31–70
Shakirin G, Hinz R, Hinz R, Kunath D, Laube K, Parodi K, Priegnitz M and Enghardt W 2011 Implementation and workflow for PET monitoring of therapeutic ion irradiation: a comparison of in-beam, in-room, and off-line techniques *Phys. Med. Biol.* **56** 1281–95
Shopa R Y *et al* 2021 Optimization of the event-based TOF filtered back-projection for online imaging in total-body J-PET *Med. Image Anal.* **73** 102199
Tashima H *et al* 2016 Development of a small single-ring OpenPET prototype with a novel transformable architecture *Phys. Med. Biol.* **61** 1795–808
Tashima H *et al* 2020 Development of a multiuse human-scale single-ring OpenPET system *IEEE Trans. Radiat. Plasma Med. Sci.* **5** 807–16
Toramatsu C *et al* 2018 Washout effect in rabbit brain: in-beam PET measurements using 10C, 11C and 15O ion beams *Biomed. Phys. Eng. Express* **4** 035001

Toramatsu C et al 2022 Measurement of biological washout rates depending on tumor vascular status in 15O in-beam rat-pet *Phys. Med. Biol.* **67** 125006

Wang Y, Seidel J, Tsui B M W, Vaquero J J and Pomper M G 2006 Performance evaluation of the GE healthcare eXplore VISTA dual-ring small-animal PET scanner *J. Nucl. Med.* **47** 1891–900

Yamaya T, Inaniwa T, Minohara S, Yoshida E, Inadama N, Nishikido F, Shibuya K, Lam C F and Murayama H 2008 A proposal of an open PET geometry *Phys. Med. Biol.* **53** 757–73

Yan J W et al 2023 Real-time digital signal processing implementation for in-beam PET of radiotherapy imaging in HIMM *Nucl. Instrum. Methods Phys. Res.* A **1045** 167545

Yang D, Cheng X and Shao Y 2021 Development and evaluation of a PET dedicated for on-line imaging and proton beam-range measurement *2021 IEEE Nuclear Science Symp. and Medical Imaging Conf. (NSS/MIC)* (IEEE) pp 1–3

Yang D, Zhu X R, Chen M, Ma L, Cheng X, Grosshans D R, Lu W and Shao Y 2024 Investigation of intra-fractionated range-guided adaptive proton therapy: (Part I) On-line PET imaging and range measurement *Phys. Med. Biol.* **69** 155005